mRMR-Tri-ConcaveHull Detector for Floating Small Targets in Sea Clutter

Yanling Shi and Yuefeng Hu

***Abstract*—For the feature-based detector of small targets in sea clutter, on the one hand, the three-dimensional convex hull-based detector deviates from the distribution of sea clutter vectors in the feature space and only combines the information of low-dimensional features. On the other hand, the redundancy and correlation between high-dimensional features are high. Consequently, we propose a detector for detecting small floating targets in sea clutter in high-dimensional feature space (HDFS) in this article. First, the maximum relevance-minimum redundancy (mRMR) algorithm to choose the low-relatedness features from the HDFS is proposed. For the mRMR algorithm, we choose the target features and sea clutter features from the eight-dimensional feature space (8-DFS), where the target features and sea clutter features have the highest degree of discrimination in the 3-DFS. Second, the distribution of sea clutter in the 3-DFS is concave or convex, which depends on the selection of features. In most cases, the distribution is concave. Using the traditional convex hull to match the concave distribution of sea clutter inevitably enlarges the judgment area and considerably decreases the detection probability. Due to the concave distribution of sea clutter in the 3-DFS, we propose a new false alarm controllable three-dimensional concave hull detector based on the mRMR (mRMR-Tri-ConcaveHull detector). In the mRMR-Tri-ConcaveHull detector, the feature vectors in the 3-DFS, which are selected by mRMR, form a concave area that is more suitable for the Concave Hull detector. Through the experimental analysis of the measured data, we find that the proposed mRMR-Tri-ConcaveHull in this article can significantly enhance the detection performance compared with the three-feature convex hull detector.**

***Index Terms*—Concave hull detector, maximum relevance-minimum redundancy (mRMR), radar, sea clutter, target detection.**

I. Introduction

THE detection of small floating targets in sea clutter has been a recent focus in the radar detection field. Due to the small radar cross section (RCS) and weak energy of small floating targets, traditional energy-based detectors often have a low detection probability [1], [2], [3], [4], [5], [6]. The nonenergy feature detector is an efficient alternative to the low signal-to-clutter ratio [7], [8].

Manuscript received 7 May 2023; revised 2 July 2023; accepted 14 July 2023. Date of publication 21 July 2023; date of current version 31 July 2023. *(Corresponding author: Yanling Shi.)*

The authors are with the College of Telecommunications and Information Engineering, Nanjing University of Post and Telecommunications, Nanjing 210003, China (e-mail: ylshi@njupt.edu.cn; 2351604359@qq.com).

Digital Object Identifier 10.1109/JSTARS.2023.3297278

By using a single feature, numerous feature-based detectors have considered the various features in several transform domains to distinguish targets from sea clutter. For example, due to the irregularity and coarseness of the amplitude of sea clutter in the time domain, sea clutter exhibits multifractal behavior [9], [10]. Hu et al. [9] proposed the Hurst exponent detector in the time domain , and Chen et al. [11] proposed a fractal-based detector for moving targets in the fractional Fourier transform domain. In addition, Li and Shui [12] proposed the normalized Doppler power spectrum detector in the frequency domain, which is superior to fractal-based detectors in terms of detecting small floating targets in sea clutter. Jin et al. [13] proposed the spectral kurtosis detector, which has demonstrated good performance when the target's Doppler frequency is outside the strong clutter area. However, the abovementioned fractal-based and feature-based detectors not only require a long time series but also ignore the nonstationary characteristics of sea clutter. To mitigate this nonstationarity, Shi et al. [14] proposed a speckle consistency factor detector that has good performance over feature-based detectors. However, single feature-based detectors have restricted detection probability because of the limited number of features utilized when dealing with different sea conditions.

Subsequently, an increasing number of features have been developed, and feature joints have been considered as candidates to improve detection performance. Shui et al. [15] proposed the convex hull detector in the three-dimensional feature space (3-DFS) based on the amplitude and Doppler spectrum, and it creates a precedent for convex hull detection. On the heels of the convex hull detector in the time and frequency domain, Shi and Shui [16] proposed another convex hull detector based on ridge integration (RI), maximum size of connected regions (MS), and number of connected regions (NR) in the time-frequency space. By comparing the detection results of [15] and [16], it is found that the three features in [16] perform well on most datasets except in a very few datasets. To further improve the detection performance, high-dimensional feature joint detection is an inevitable trend. However, it is painful to break through the 3-DFS, and for the convex hull, it is difficult to design the convex hull detector in a high-dimensional feature space (HDFS). Therefore, both Shui et al. [17] proposed feature compression based on the Bhattacharyya distance, and Gu [18] used principal component analysis by converting from a HDFS to 3-DFS. Compared with previous detectors based on a single feature or three features, the detectors in [17] and [18] have achieved a better detection

performance with an inevitable compression loss. In order to achieve fast learning and decision and strong generalizability, Guo et al. [19] proposed a fast feature-fusion-based detector, which combines the nonlinear transformations to normalize the features of sea clutter with the optimal feature fusion. In addition, the distribution of sea clutter in the 3-DFS is concave or convex, which depends on the selection of features. In most cases, the distribution is concave. Using the traditional convex hull to match the concave distribution of sea clutter in the 3-DFS necessarily enlarges the judgment area and greatly drops the detection probability.

In recent years, scholars have tried to combine radar target detection with machine learning. Li et al. [20] extracted three features, the time information entropy, the time Hurst index, and the frequency peak-to-average ratio, built a 3-DFS, and used the support vector machine (SVM) to achieve the desired false alarm controllable (FAC) detector. To combine more features, Guo and Shui [21] proposed the K nearest neighbor (KNN) with FAC to detect small surface targets in sea clutter, which effectively improves the detection performance in HDFS. However, KNN-FAC is coarse when selecting the number of nearest neighbors, and its detection performance is limited [21]. Convolutional neural networks (CNNs) have a wide range of applications in image recognition and classification. They can make full use of the local features of datasets, have strong generalization ability, and share the available weights to simplify the network structure [22], [23], [24]. Bringing the CNN into the target detection field, Shi et al. [25] proposed the CNN-FAC by using recursive plots of sea clutter and targets and noted the direction of target detection with the CNN.

The distribution of sea clutter vectors in the feature space can be convex or concave. If the distribution is concave, the concave hull can wrap the feature vectors more compactly than the convex hull. In this way, the concave judgment area is more in line with the actual situation, and the detection probability is successfully enhanced. With an N-dimensional concave hull (N-D concave hull) algorithm, Li and Niggemann [26] converted a convex hull into a concave hull in any dimension space and applied the N-D concave hull to fan fault diagnosis. Inspired by Peng's idea, we apply the idea of concave hulls to the target detector based on the three features. However, we also face three problems concurrently: first, before forming the judgment area, we need to delete the false alarm points according to the principle of maximum volume loss of concave hulls. However, deleting the false alarm points using the concave hull of [26] can result in high algorithm complexity. To solve this problem, we introduce the fast FAC alpha concave hull. Based on the principle of maximum volume loss of concave hulls, the false alarm points are deleted one by one according to the false alarm rate. Therefore, we achieve accurate control of the false alarm rate. Second, the execution efficiency of the N-D concave hull in [26] is not high. Instead, we choose to change the selection method of internal digging points to accelerate. Third, some internal points may be located outside the concave hull after internal digging, which leads to the failure of the constant false alarm rate (CFAR) in the final judgment area. To solve this problem, we introduce the external filling algorithm in [27] after each internal digging operation. Therefore, we propose a Tri-ConcaveHull detector with a controllable false alarm.

In the age of big data, the volume and dimensions of data are increasing, and extracting features with large gaps from HDFS is a crucial problem. Feature selection is currently an effective dimensionality reduction technology. It reduces the dimension by removing the relevant and redundant features while retaining the irrelevant features to form the optimal feature set [28], [29], [30], [31]. Peng et al. [32] proposed the maximum relevance-minimum redundancy (mRMR) algorithm by calculating mutual information (MI), which is an optimal feature selection method based on MI theory. The mRMR is relatively simple and has the advantages of low data requirements and high computing efficiency [33], [34]. Therefore, we use mRMR to select the three optimal features from HDFS. Combining the mRMR with the Tri-ConcaveHull detector, the proposed detector is called the mRMR-Tri-ConcaveHull detector with a controllable false alarm.

Because in most cases, the distribution of sea clutter in the 3-DFS is concave, using the traditional convex hull to match the concave distribution of sea clutter inevitably enlarges the judgment area and considerably decreases the detection probability. In addition, utilizing high-dimensional feature information is the current and future trend in the detection of floating small targets in sea clutter. In conclusion, the motivation of this article is to fit the concave distribution of sea clutter and to reduce the dimension in the high dimensional space. On the one hand, the use of FAC Tri-ConcaveHull detector matches the concave distribution of sea clutter more closely than the traditional convex hull, thus reducing the area of judgment. On the other hand, we use the mRMR to select 3-D features from 8-DFS as the input of the FAC Tri-ConcaveHull detector, so that the target features and sea clutter features have the highest recognition in 3-DFS.

The innovation of this article is that we first propose a new FAC Tri-ConcaveHull detector for floating small targets in sea clutter, which not only meets the requirements of the controllable false alarm but also wraps the feature vectors more compactly than the convex hull. To further improve the detection probability, the mRMR is used to obtain the optimal feature set with the minimum redundancy between internal features and the maximum relevance between internal features and stability label vectors. The feature set is input to the FAC Tri-ConcaveHull detector to achieve high detection performance. The experimental results show that the detection performance of the proposed mRMR-Tri-ConcaveHull detector is significantly improved.

This article is organized as follows: Section II introduces the signal detection model and eight features; Section III introduces the feature selection algorithm, including the mRMR; Section IV introduces the target detection algorithm, including the 3-D FAC convex hull learning algorithm and 3-D FAC concave hull learning algorithm, and proposes the mRMR-Tri-ConcaveHull detector; Section V verifies the effectiveness of the proposed mRMR-Tri-ConcaveHull detector through experiments; and Section VI concludes the article.

II. Signal Detection Model and Eight Features

The following binary hypothesis test model [35] can be used to judge whether the radar received echo contains targets

$$\begin{cases} H_0: \begin{cases} \boldsymbol{x} = \mathbf{c} \\ \tilde{\boldsymbol{x}}_k = \mathbf{c}_k, k = 1, \ldots, K \end{cases} \\ H_1: \begin{cases} \boldsymbol{x} = \mathbf{s} + \mathbf{c} \\ \tilde{\boldsymbol{x}}_k = \mathbf{c}_k, k = 1, \ldots, K \end{cases} \end{cases}. \tag{1}$$

In formula (1), under the null hypothesis H_0, the received $N-$dimensionalpulse-echo data, $\boldsymbol{x} \in \mathrm{C}^{N\times 1}$, $\boldsymbol{x} = \{x_1, x_2, \ldots, x_N\}^T$,consist of only clutter $\mathbf{c}$, which means that there is no target at the cell under test (CUT). Under the alternative hypothesis H_1, the received N-dimensional pulse-echo data $\boldsymbol{x}$ contains not only clutter $\mathbf{c}$ but also target signal $\mathbf{s}$, and $\mathbf{s}$ is statistically independent of $\mathbf{c}$. $\tilde{\boldsymbol{x}}_k \in \mathrm{C}^{N\times 1}, \tilde{\boldsymbol{x}}^k = \{\tilde{x}_{1,k}, \tilde{x}_{2,k}, \ldots, \tilde{x}_{N,k}\}$ is the N-dimensional pulse-echo data of the kth reference cell around the CUT, consisting of only clutter, and K is the number of reference cells.

The received radar echo data contain some rich information that can be characterized using several features to distinguish sea clutter and targets. Next, we introduce eight features used in the field of small target detection in sea clutter. The eight features are the normalized Hurst exponent (NHE) [36], relative average amplitude (RAA), relative Doppler peak height (RDPH), relative vector entropy (RVE) [15], RI, maximum size of connected regions (MS), number of connected regions (NR) [16], the normalized sample covariance matrix and the generalized likelihood ratio test (NSCM-GLRT) [37]. Among them, the NHE and RAA are amplitude features, the RDPH and RVE are Doppler features, the RI, MS, and NR are time-frequency features, and the NSCM-GLRT is a statistical feature.

The above eight-dimensional (8-D) features are extracted from the received echo to form the 8-D feature vector $\boldsymbol{\mu}$. The 8-D clutter feature vector and the 8-D feature vector at the CUT are defined as follows:

$$\boldsymbol{\varsigma} = \boldsymbol{\mu}(x\,|H_0\,) \tag{2}$$

$$\boldsymbol{\kappa} = \boldsymbol{\mu}(x\,|H_1\,). \tag{3}$$

Next, we use feature selection on the extracted 8-D feature vectors for the conversion from HDFS to 3-DFS.

III. Algorithm of Optimal Feature Selection: mRMR

To select the optimal 3-D feature vectors with the largest gaps between the target and sea clutter from the multidimensional feature vectors, the mRMR is used to obtain the optimal feature set with the minimum redundancy between the internal features and the maximum relevance between the internal features and stability label vectors [32], [33], [34].

The mRMR is based on MI defined as follows:

$$\mathrm{MI}(\boldsymbol{A};\boldsymbol{B}) = \sum_{A\in A}\sum_{B\in B} p(A,B)\log_2\frac{p(A,B)}{p(A)p(B)} \tag{4}$$

where A is an element belonging to $\boldsymbol{A}$, B is an element belonging to $\boldsymbol{B}$, $p(A, B)$ is the joint probability density function of A and B, and $p(A)$ and $p(B)$ are the probability density functions of A and B, respectively. When two random variables are completely independent, the MI is 0.

In this article, the mRMR is used to select the optimal 3-D feature vectors. First, the set $\{\varsigma_1; \ldots; \varsigma_Q\}$ of 8-D clutter feature vectors and the set $\{\boldsymbol{\kappa}_1; \ldots; \boldsymbol{\kappa}_T\}$ of 8-D feature vectors at the CUT are spliced into a matrix, as shown in the following formula:

$$\boldsymbol{R}_G = [\boldsymbol{\varsigma}_1; \ldots; \boldsymbol{\varsigma}_Q; \boldsymbol{\kappa}_1; \ldots; \boldsymbol{\kappa}_T] \tag{5}$$

where Q is the total number of sea clutter samples, and T is the total number of samples at the CUT.

Formula (5) is also equivalent to a set of 1-D feature vectors and is defined as follows:

$$\boldsymbol{R}_G = \{\boldsymbol{a}_1, \ldots, \boldsymbol{a}_j, \ldots, \boldsymbol{a}_8\} \tag{6}$$

where $\boldsymbol{a}_j$ is the 1-D feature vector that contains $Q + T$ samples in set $\boldsymbol{R}_G$.

Suppose $\boldsymbol{G}$ is a subset of $\boldsymbol{R_G}$ and is defined as follows:

$$\boldsymbol{G} = \left\{\boldsymbol{g}_1, \ldots, \boldsymbol{g}_i, \ldots, \boldsymbol{g}_{|\boldsymbol{G}|}\right\} \tag{7}$$

where $\boldsymbol{g}_i$ is the 1-D feature vector containing $Q + T$ samples in set $\boldsymbol{G}$, $|\boldsymbol{G}|$ is the number of 1-D feature vectors contained in $\boldsymbol{G}$.

The incremental search is used in the mRMR to sort all feature vectors, as shown in Algorithm 1.

Algorithm 1: mRMR.

Input: $\boldsymbol{R_G}$, $\boldsymbol{b}$
Output: $\boldsymbol{\xi}_{\text{opt}}$, $\boldsymbol{\eta}_{\text{opt}}$
1. Initialization $\mathrm{s}' = 1$
2. for$(j = 1\text{to}8)$do
3. Based on the mutual information definition in formula (4), calculate the relevance between $\boldsymbol{a}_j$ and $\boldsymbol{b}$;
4. end for
5. Add the most relevant vector in $\boldsymbol{R}_G$ to set $\boldsymbol{G}$, where $\boldsymbol{G} = \{\boldsymbol{g}_1\}$;
6. for$(\mathrm{s}' = 2\text{to}3)$do
7. Using the existing element $\boldsymbol{g}_i$ in set $\boldsymbol{G}$, add the feature vector $\boldsymbol{g}_{s'}$ satisfying (8);

$$\boldsymbol{g}_{s'} = \underset{a_j\in R_G - G}{\arg\max}\left[\frac{\mathrm{MI}(\boldsymbol{a}_j;\boldsymbol{b})}{\frac{1}{|\boldsymbol{G}|}\sum_{\boldsymbol{g}_i\in\boldsymbol{G}}\mathrm{MI}(\boldsymbol{a}_j;\boldsymbol{g}_i)}\right] \tag{8}$$

8: end for
9: Separate the set G into the optimal 3-D clutter feature vectors $\boldsymbol{\xi}_{\text{opt}}$ and optimal 3-D feature vectors at the CUT $\boldsymbol{\eta}_{\text{opt}}$;
10: return$\boldsymbol{\xi}_{\text{opt}}$, $\boldsymbol{\eta}_{\text{opt}}$

In Algorithm 1, we input $\boldsymbol{R_G}$ and stability label vector $\boldsymbol{b}$, select the features of $\boldsymbol{R_G}$ according to the mRMR, and obtain its optimal subset $\boldsymbol{G}$. Since an optimal 3-D feature vector is required, the value of the final $|\boldsymbol{G}|$ is 3. Finally, the subset $\boldsymbol{G}$ is separated into optimal 3-D clutter feature vectors $\boldsymbol{\xi}_{\text{opt}}$ and optimal 3-D feature vectors at the CUT $\boldsymbol{\eta}_{\text{opt}}$, where each optimal 3-D clutter feature vector $\boldsymbol{\xi}_{\text{opt}}$ represents one clutter sample in the 3DFS, and each optimal 3-D feature vector at the CUT $\boldsymbol{\eta}_{\text{opt}}$ represents one sample of the CUT in the 3DFS.

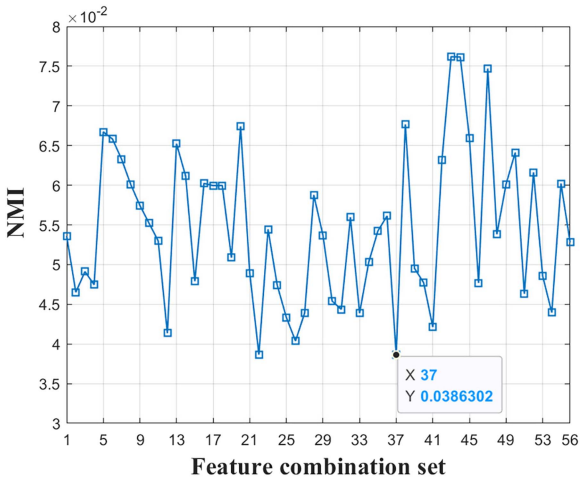

Fig. 1. NMI s of 56 combinations of the 3-D feature vectors.

To evaluate the optimality of the selected 3-D feature vector, the normalized MI metric NMI is used as the measure index. First, the MI metric is defined as follows:

$$\mathrm{MI}(\boldsymbol{\xi},\boldsymbol{\eta}) = \sum_{\xi\in\boldsymbol{\xi}}\sum_{\eta\in\boldsymbol{\eta}} p(\xi,\eta)\log_2\frac{p(\xi,\eta)}{p(\xi)p(\eta)} \tag{9}$$

where $p(\xi)$ is the probability of data ξ in 3-D clutter feature vectors $\boldsymbol{\xi}$, $p(\eta)$is the probability of data η in 3-D feature vectors at the CUT $\boldsymbol{\eta}$, and $p(\xi,\eta)$ is the joint probability of ξ and η. Then, the normalized MI metricNMI is defined as follows:

$$\mathrm{NMI}(\boldsymbol{\xi},\eta) = \frac{\mathrm{MI}(\boldsymbol{\xi},\boldsymbol{\eta})}{\sqrt{H(\boldsymbol{\xi})*H(\eta)}} \tag{10}$$

where$H(\boldsymbol{\xi})$ and $H(\boldsymbol{\eta})$ are the information entropies of $\boldsymbol{\xi}$ and $\boldsymbol{\eta}$, respectively, which are defined as follows:

$$H(\boldsymbol{\xi}) = -\sum_{\xi\in\boldsymbol{\xi}} p(\xi)\log_2 p(\xi) \tag{11}$$

$$H(\boldsymbol{\eta}) = -\sum_{\eta\in\boldsymbol{\eta}} p(\eta)\log_2 p(\eta). \tag{12}$$

If the correlation between $\boldsymbol{\xi}$ and $\boldsymbol{\eta}$ is weaker, the value of NMI is smaller. It is known that there are $C_8^3 = 56$ combinations when 3-D feature vectors are selected from 8-D feature vector space. Fig. 1 shows the NMIs of 56 combinations.

From Fig. 1, the 37th combination is selected by the mRMR. The NMI of the 3-D feature vector selected by the mRMR is less than the other 3-D feature vectors, which proves that there is the weakest correlation between the 3-D clutter feature vector and the 3-D feature vector at the CUT selected by the mRMR. This result conforms to the required principle of feature selection.

IV. Target Detection Algorithm

After obtaining the 3-D feature vectors, we can transform the detection into a single classification or anomaly detection. The 3-D clutter feature vectors $\boldsymbol{\xi}_q$ form a set $\boldsymbol{\zeta} = \{\boldsymbol{\xi}_q \in R^3, q = 1,\ldots,Q\}$, where Q is the total number of clutter feature vectors. The judgment area of detection is an area that can wrap those clutter feature vectors tightly. During the decision stage, if the feature vector at the CUT falls inside the judgment area of detection, then there is no target. Otherwise, if the feature vector falls outside the judgment area, there is a target.

According to the Neyman-Pearson criterion, in the 3-DFS, when the conditional probability densities $p(\boldsymbol{\xi}|H_1)$ and $p(\boldsymbol{\xi}|H_0)$ of H_1 and H_0 are known and the false alarm rate P_F is given, where P_F refers to the probability of clutter being misjudged as the target, the judgment area Ω of detection can be expressed as follows:

$$\max_{\Omega}\left\{P_D = 1 - \iiint_{\Omega} p(\boldsymbol{\xi}|H_1)d\xi\right\},$$
$$\text{s.t.} \iiint_{\Omega} p(\boldsymbol{\xi}|H_0)dx = 1 - P_F \tag{13}$$

where P_D is the detection probability. According to [15], Ω is a limited space, and it is assumed that the judgment area is contained in a larger uniform distribution space. The final judgment area can be simplified into an optimization problem as follows:

$$\min_{\Omega\in\boldsymbol{C}}\{|\Omega|\},\ \text{s.t.}\ \frac{\#\{q,\boldsymbol{\xi}_q\in\Omega\}}{Q} = 1 - P_F \tag{14}$$

where $\boldsymbol{C}$ represents all bounded sets in R^3, which can be convex or concave, and $\#\{q,\boldsymbol{\xi}_q\in\Omega\}$ is the number of clutter feature vectors in the judgment area. By solving the optimization, the judgment area can be obtained. When the judgment area Ω is a convex space, the detection is called convex hull detection; when the judgment area Ω is a concave space, the detection is called concave hull detection. Next, we introduce convex hull detection and concave hull detection.

A. 3-D FAC Convex Hull Learning Algorithm

The 3-D FAC convex hull learning algorithm [15] uses the convex hull to wrap the clutter feature vectors. Thus, the judgment area is convex. The solution to formula (14) involves finding the convex hull with the following two conditions: the volume of the convex hull is at a minimum, and the number of clutter feature vectors wrapped by the convex hull is $[(1-P_F)\times Q]$. We use the convex hull learning algorithm to obtain the optimal solution in which the clutter feature vectors are regarded as training sample points in the 3-DFS. The 3-D FAC convex hull learning algorithm is used to obtain the convex judgment area $\Omega_{\text{convexhull}}$. During the decision stage, if the feature vectors at the CUT fall inside the judgment area of detection, then there are no targets. Otherwise, if the feature vectors fall outside the judgment area, these are considered targets. When the distribution of $\boldsymbol{\zeta}$ in the 3-D space is convex, the convex hull learning algorithm exhibits good detection performance. However, in practical applications, the distribution of $\boldsymbol{\zeta}$ in the 3-D space is not always convex and is often concave. In this case, if the convex hull learning algorithm is still used, the judgment area will inevitably extend, and the detection performance will inevitably be lost. Therefore, in the next section, we study the concave hull learning algorithm with the concave distribution of $\boldsymbol{\zeta}$ in 3-D space.

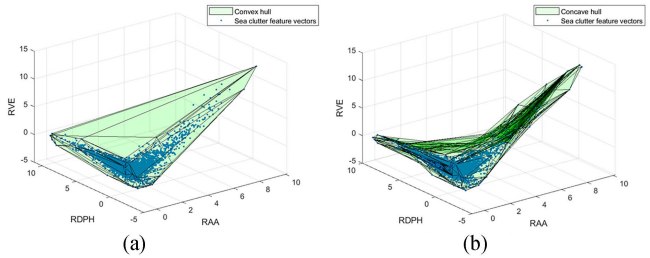

Fig. 2. Distribution of sea clutter feature vectors in 3-D space. (a) Convex hull algorithm. (b) Concave hull algorithm.

B. Proposed 3-D FAC Concave Hull Learning Algorithm

According to the above, formula (14) is obtained on the premise that the judgment area is a uniformly distributed space. In fact, due to the obvious gaps in the convex hull, the distribution of the sea clutter feature vectors is usually not uniform. Fig. 2 shows the convex hull, the concave hull, and the distribution of sea clutter feature vectors in 3-D space. As shown in Fig. 2(a), there are large gaps. When the feature vectors at the CUT fall in these gaps, they will be incorrectly judged as clutter feature vectors. However, these gaps are formed by the connection of the vertices in the convex hull and do not contain sea clutter feature vectors. If a convex hull with large gaps is considered the judgment area, it will inevitably lead to a considerable detection error. If these gaps are removed and a new judgment area is formed, as shown in Fig. 2(b), the judgment area will become a concave hull with a smaller volume than the convex hull. In addition, the concave hull can wrap the sea clutter feature vectors more compactly, so the detection performance will be better.

It can be seen from Fig. 2 that there are a large number of gaps in the convex hull without sea clutter, which will inevitably reduce the detection probability. The concave hull encloses the sea clutter feature vectors more compactly, which effectively reduces the gap and makes the judgment area more reasonable. For this reason, we propose a 3-D FAC concave hull learning algorithm, as shown in Algorithm 2. It comprises five parts: delete false alarm points by the alpha concave hull, form the convex hull by $\boldsymbol{\zeta}_{Nf}$, carry out the concave hull internal digging algorithm, carry out the concave hull external filling algorithm, and obtain the final concave judgment area Ω_{final}.

Li and Niggemann [26] present an $N-$ dimensional concave hull algorithm that can form a concave hull in any dimensional space. In the field of radar detection, it is very difficult to control false alarms in high-dimensional space. Therefore, we reduce the HDFS to 3-DFS first, which is realized in Section III, and we use the internal digging algorithm to achieve 3-D concave hull feature detection. However, there are three troubles encountered when using this algorithm in [26] to form a judgment area.

First, to form the judgment area, we need to delete the false alarm points according to the principle of maximum volume loss of concave hulls. However, deleting the false alarm points using the concave hull from [26] can result in high algorithm complexity. To reduce the algorithm complexity, we introduce the fast FAC alpha concave hull. As shown in Algorithm 3's table, similar to the convex hull learning algorithm and based on the principle of the maximum reduction of the alpha concave volume, we obtain the updated clutter feature vector set $\boldsymbol{\zeta}_{N_f}$ by iteratively deleting $[P_F \times Q]$ false alarm points from the clutter feature vector set $\boldsymbol{\zeta}$.

Algorithm 2: 3-D FAC Concave Hull Learning Algorithm.

Input: $\boldsymbol{\zeta}$, P_F
Output: final concave judgment area Ω_{final}
1. Algorithm 3: Use the fast FAC alpha concave hull to delete false alarm points and get $\boldsymbol{\zeta}_{Nf}$;
2. According to $\boldsymbol{\zeta}_{Nf}$, the original convex hull Ω_{original}, whose surface is composed of D triangulation planes, is generated by the convex hull algorithm;
3. Calculate the perimeter $L_d, d = 0, \ldots, D$ of all triangulation planes;
4. Calculate the average perimeter of all triangulation planes and use it as the $threshold$;
5. Initialize $i = 1, j = 1, \Omega_{i,j} = \Omega_{\text{original}}$ and the number of internal digging operations $dig\_num = 150$;
6. while $(j \leq dig\_num)$ do
7. Calculate the perimeter $L_{j,d}, d = 0, \ldots, D$ of all triangulation planes of $\Omega_{i,j}$;
8. Calculate the maximum value $L_{j,\max}$ in $L_{j,d}$, $d = 0, \ldots, D$;
9. if $(L_{j,\max} > threshold)$ then
10. Algorithm 4: Concave hull internal digging algorithm, $i = i + 1, j = j$, get $\Omega_{i,j}$;
11. Algorithm 5: Concave hull external filling algorithm, $j = j + 1, i = i$, get $\Omega_{i,j}$;
12. else
13. break;
14. end if
15. end while
16. $\Omega_{\text{final}} = \Omega_{i,j}$;
17. return Ω_{final};

Second, the internal digging point selected in [26] is the nearest internal point to the edge $side$, which results in an inefficient internal digging operation. To solve this problem, we select the inner point nearest to the center point of the edge $side$ as the internal digging point and improve the concave hull internal digging algorithm, as shown in Algorithm 4.

Third, in Algorithm 4, after each internal digging operation, there may be some internal points located outside the concave hull, resulting in a final generated judgment area that does not satisfy the CFAR. To solve this problem, the external filling algorithm from [27] is introduced after each internal digging operation, as shown in Algorithm 5.

Based on the above three improvements, we can obtain the proposed 3-D FAC concave hull learning algorithm in this article. The flow chart is shown in Fig. 3.

A concave hull is formed by internal digging and external filling on the basis of a convex hull. The process of forming a concave hull after each internal digging and external filling is shown in Fig. 4.

Algorithm 3: Use the Fast FAC Alpha Concave Hull to Delete the False Alarm Points.

Input: $\boldsymbol{\zeta}$, P_F
Output: $\boldsymbol{\zeta}_{N_f}$
1. Calculate the number of sample points Q in set $\boldsymbol{\zeta}$;
2. Calculate the number of false alarm points $N_f = Q \times P_F$;
3. Initialize $v = 1$, $\boldsymbol{\zeta}_v = \boldsymbol{\zeta}$;
4. while $(v \leq N_f)$ do
5. Generate the fast FAC alpha concave hull of $\boldsymbol{\zeta}_v$ and calculate its volume;
6. When one concave hull's vertex is deleted from $\boldsymbol{\zeta}_v$, calculate the volume of the concave hull with the remaining sample points;
7. Record the vertex of the concave hull that can maximumly reduce the volume of the concave hull;
8. Delete this vertex from set $\boldsymbol{\zeta}_v$, $v = v + 1$, get a new $\boldsymbol{\zeta}_v$;
9. end while
10. $\boldsymbol{\zeta}_{N_f} = \boldsymbol{\zeta}_v$;
11. return $\boldsymbol{\zeta}_{N_f}$;

Algorithm 4: Concave Hull Internal Digging Algorithm.

Input: $\Omega_{i,j}$
Output: Update $\Omega_{i,j}$ by internal digging
1. Find the triangulation plane $\Delta_{m1,i}$ corresponding to $L_{j,\max}$;
2. Find the longest edge $side$ in $\Delta_{m1,i}$;
3. Get another triangulation plane $\Delta_{m2,i}$ that shares the same edge $side$ with $\Delta_{m1,i}$;
4. Use the points that are not the vertices about $\Omega_{i,j}$ as the interior points;
5. Find the internal digging point P_0 that is closest to the center point of the edge $side$ from the interior points;
6. Let all vertices of $\Delta_{m1,i}$ and $\Delta_{m2,i}$ be point set F;
7. Create new facets $\Delta_{1,i}, \Delta_{2,i}, \Delta_{3,i}, \Delta_{4,i}$ using point set $\boldsymbol{F}$ and P_0 and satisfy:

$$\{\Delta_{1,i}, \Delta_{2,i}, \Delta_{3,i}, \Delta_{4,i}\} \cap \{\Delta_{m1,i}, \Delta_{m2,i}\} = \emptyset \quad (15)$$

8: Delete $\Delta_{m1,i}, \Delta_{m2,i}$ from $\Omega_{i,j}$ and add $\Delta_{1,i}, \Delta_{2,i}, \Delta_{3,i}, \Delta_{4,i}$ to complete the update. From a spatial point of view, the hexahedron composed of $\Delta_{1,i}, \Delta_{2,i}, \Delta_{3,i}, \Delta_{4,i}, \Delta_{m1,i}, \Delta_{m2,i}$ is dug out in space $\Omega_{i,j}$;
9: return $\Omega_{i,j}$;

Fig. 4 shows that from the perspective of space, one internal digging operation is equivalent to digging out a hexahedron in space $\Omega_{i,j}$, and one external filling operation is equivalent to filling a tetrahedron in space $\Omega_{i,j}$.

Both the fast FAC alpha concave hull and the concave hull formed by Algorithms 4 and 5 have their own advantages and disadvantages. For the former, the computational complexity of the concave volume is low, but the generated concave hull

Algorithm 5: Concave Hull External Filling Algorithm.

Input: $\Omega_{i,j}$
Output: Update $\Omega_{i,j}$ by external filling
1. Use the clutter feature vectors outside $\Omega_{i,j}$ to form a set $\boldsymbol{Z} = \{Z_1, \ldots, Z_H\}$. H is the number of clutter feature vectors outside $\Omega_{i,j}$;
2. for $(t = 1$ to $4)$ do
3. for $(h = 1$ to $H)$ do
4. Calculate the distances from Z_h to $\Delta_{1,i}$, $\Delta_{2,i}$, $\Delta_{3,i}$, $\Delta_{4,i}$, which are di_1, di_2, di_3, di_4, respectively;
5. if $(di_t = \min\{di_1, di_2, di_3, di_4\})$ then
6. Store Z_h in set $\boldsymbol{J}_s$;
7. end if
8. end for
9. Sort the points in $\boldsymbol{J}_s$ from near to far from $\Delta_{t,i}$ to get a new set $\boldsymbol{J'}_s = \{J'_1, \ldots, J'_S\}$. S is the number of points in set $\boldsymbol{J}_s$;
10. for$(s = 1$ to $S)$ do
11. Among all triangulation planes of the $\Omega_{i,j}$ surface, find the closest triangulation plane Δ_{near} to J'_s;
12. Let all vertices of Δ_{near} be point set $\boldsymbol{F'}$;
13. Use point set $\boldsymbol{F'}$ and point J'_s to create new faces $\Delta_{5,j}, \Delta_{6,j}, \Delta_{7,j}$ and satisfy:

$$\{\Delta_{5,j}, \Delta_{6,j}, \Delta_{7,j}\} \cap \{\Delta_{near}\} = \emptyset \quad (16)$$

14: Delete Δ_{near} from $\Omega_{i,j}$, add $\Delta_{5,j}, \Delta_{6,j}, \Delta_{7,j}$, and complete the update of $\Omega_{i,j}$. From the perspective of space, it is equivalent to the $\Omega_{i,j}$ space filled by tetrahedron PO_{fill} composed of $\Delta_{5,j}, \Delta_{6,j}, \Delta_{7,j}, \Delta_{near}$;
15: end for
16: end for
17: return $\Omega_{i,j}$;

volume is larger than the latter. For the latter, although its volume is smaller than the former, its computational complexity is higher. Therefore, we introduce the fast FAC alpha concave hull to update the sea clutter feature vector set, as shown in Fig. 3. The $[P_F \times Q]$ false alarm points are deleted from the clutter feature vector set by iteration according to the principle of the maximum reduction of the concave hull volume. Then, the updated clutter feature vector set is used to generate a convex hull. On the basis of the convex hull, Algorithms 4 and 5 are used to generate the final concave judgment area Ω_{final}.

C. Proposed mRMR-Tri-ConcaveHull Detector

Combining the contents in Sections III and IV-B, the flow chart of the mRMR-Tri-ConcaveHull detector is shown in Fig. 5.

As shown in Fig. 5, first, with the received data, the features are extracted to form the 8-D clutter feature vector $\boldsymbol{\varsigma}$ and the 8-D feature vector $\boldsymbol{\kappa}$ at the CUT. Second, the two vectors are spliced to form $\boldsymbol{R}_G$. Third, the optimal 3-D clutter feature vectors $\boldsymbol{\xi}_{\text{opt}}$ and optimal 3-D feature vectors at the CUT $\boldsymbol{\eta}_{\text{opt}}$ are obtained by the mRMR algorithm. Then, $\boldsymbol{\xi}_{\text{opt}}$ are input

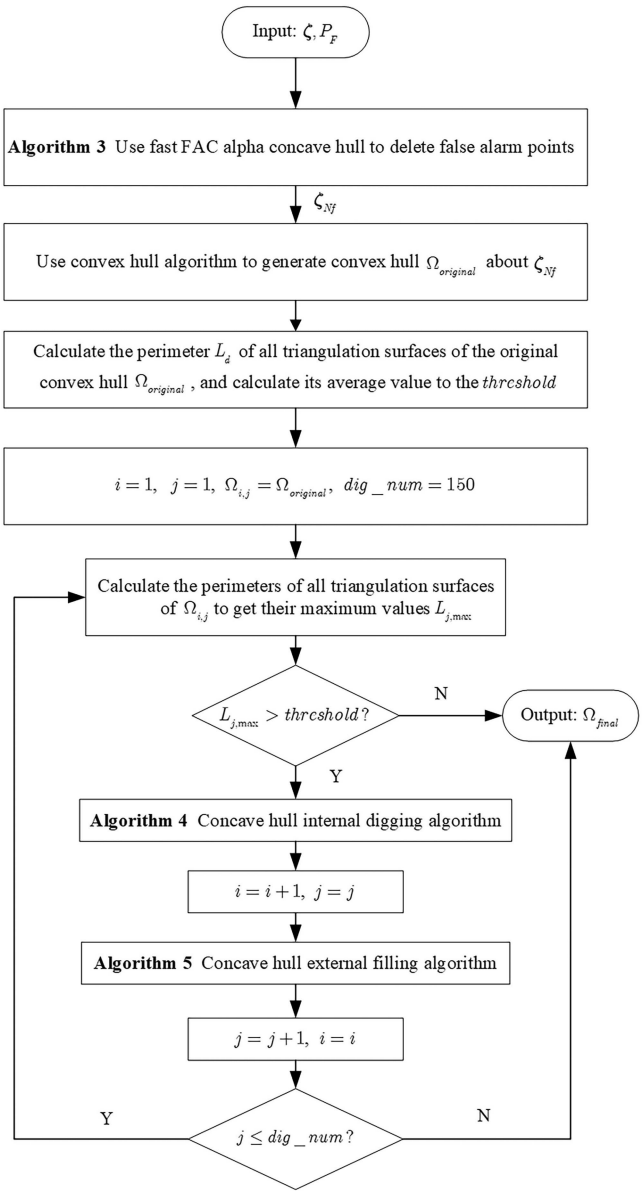

Fig. 3. Flowchart of the Algorithm 2.

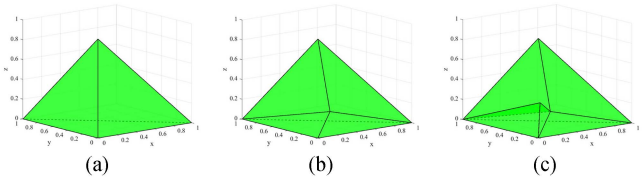

Fig. 4. Formation process of internal digging and external filling. (a) Convex hull. (b) Concave hull after one internal digging operation. (c) Concave hull after one internal digging and external filling operation.

into the proposed concave hull detector and used as training sample points. Concave hull detection can be divided into two steps: First, the judgment area Ω_{final} is obtained by the 3-D FAC concave hull learning algorithm. Second, the position of $\boldsymbol{\eta}_{\text{opt}}$ is determined with respect to the judgment area Ω_{final}. If $\boldsymbol{\eta}_{\text{opt}}$ is

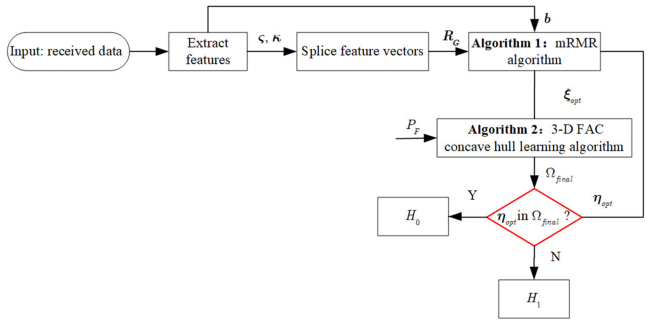

Fig. 5. Flow of the mRMR-Tri-ConcaveHull detector.

inside the judgment area Ω_{final}, it is judged as H_0; otherwise, it is judged as H_1.

It can be seen from Section IV-B that the judgment area Ω_{final} is a concave hull that is obtained by digging several hexahedrons PO_{dig} and filling several tetrahedrons PO_{fill} from Ω_{original}. The original convex hull Ω_{original}, the hexahedron PO_{dig} and the tetrahedron PO_{fill} are convex polyhedrons whose surfaces are composed of triangulation planes. Therefore, the original convex hull Ω_{original}, the hexahedron PO_{dig} and the tetrahedron PO_{fill} can be expressed as follows:

$$\Omega_{\text{original}} = SP\{\text{triangle}(u_d^{(1)}, u_d^{(2)}, u_d^{(3)}), d = 1, 2, \ldots, D\} \tag{17}$$

$$PO_{\text{dig}} = SP\{\text{triangle}\left(u\prime_d^{(1)}, u\prime_d^{(2)}, u\prime_d^{(3)}\right), d = 1, 2, \ldots, 6\} \tag{18}$$

$$PO_{\text{fill}} = SP\{\text{triangle}(u\prime_d^{(1)}, u\prime_d^{(2)}, u\prime_d^{(3)}), d = 1, 2, 3\} \tag{19}$$

where $SP\{\}$ represents the convex polyhedron formed by triangulation planes, $u_d^{(1)}, u_d^{(2)}, u_d^{(3)}$ represent the vertices of the triangulation plane of Ω_{original}, D represents the number of its triangulation planes, $u\prime_d^{(1)}, u\prime_d^{(2)}, u\prime_d^{(3)}$ represent the vertices of the triangulation plane in PO_{dig}, and $u\prime_d^{(1)}, u\prime_d^{(2)}, u\prime_d^{(3)}$ represent the vertices of the triangulation plane in PO_{fill}. We store all PO_{dig} and PO_{fill} in two sets. Therefore, we only need to judge the position of the η_{opt} corresponding to Ω_{original}, PO_{dig}, and PO_{fill} in turn. We calculate its detection statistics as follows:

$$\rho(\boldsymbol{\eta}_{\text{opt}}) = \max_d \left\{ \left| \left[u_d^{(1)} - \boldsymbol{\eta}_{\text{opt}}, u_d^{(2)} - \boldsymbol{\eta}_{\text{opt}}, u_d^{(3)} - \boldsymbol{\eta}_{\text{opt}} \right] \right|, d = 1, 2, \ldots, D \right\} \tag{20}$$

$$\rho\prime(\boldsymbol{\eta}_{\text{opt}}) = \max_d \left\{ \left| \left[u\prime_d^{(1)} - \boldsymbol{\eta}_{\text{opt}}, u\prime_d^{(2)} - \boldsymbol{\eta}_{\text{opt}}, u\prime_d^{(3)} - \boldsymbol{\eta}_{\text{opt}} \right] \right|, d = 1, 2, \ldots, 6 \right\} \tag{21}$$

$$\rho\prime(\boldsymbol{\eta}_{\text{opt}}) = \max_d \left\{ \left| \left[u\prime_d^{(1)} - \boldsymbol{\eta}_{\text{opt}}, u\prime_d^{(2)} - \boldsymbol{\eta}_{\text{opt}}, u\prime_d^{(3)} - \boldsymbol{\eta}_{\text{opt}} \right] \right|, d = 1, 2, 3 \right\}. \tag{22}$$

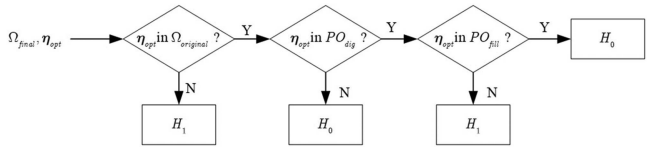

Fig. 6. Detection flow to determine whether $\boldsymbol{\eta}_{\text{opt}}$ is inside the concave judgment area Ω_{final}.

If $\rho(\boldsymbol{\eta}_{\text{opt}}) \leq 0$, then $\boldsymbol{\eta}_{\text{opt}}$ is inside Ω_{original}. Similarly, if $\rho\prime(\boldsymbol{\eta}_{\text{opt}}) \leq 0$, then η_{opt} is inside PO_{dig}. If$\rho''(\boldsymbol{\eta}_{\text{opt}}) \leq 0$, then $\boldsymbol{\eta}_{\text{opt}}$ is inside PO_{fill}.

As shown in Fig. 6, first, we judge whether $\boldsymbol{\eta}_{\text{opt}}$ is inside Ω_{original}; if not, then judge it as H_1; otherwise, continue to judge whether it is inside PO_{dig}. If not, it will be judged as H_0; otherwise, continue to judge whether it is inside PO_{fill}. If not, it will be judged as H_1; otherwise, it will be judged as H_0. The formula using detection statistics is as follows:

$$\begin{cases} H_0: \begin{cases} \rho(\boldsymbol{\eta}_{\text{opt}}) \leq 0 \text{ and } \rho'(\boldsymbol{\eta}_{\text{opt}}) > 0 \ (23.1) \\ \rho(\boldsymbol{\eta}_{\text{opt}}) \leq 0 \text{ and } \rho'(\boldsymbol{\eta}_{\text{opt}}) \leq 0 \text{ and } \rho''(\boldsymbol{\eta}_{\text{opt}}) \leq 0 \ (23.2) \end{cases} \\ H_1: \begin{cases} \rho(\boldsymbol{\eta}_{\text{opt}}) > 0 \ (23.3) \\ \rho(\boldsymbol{\eta}_{\text{opt}}) \leq 0 \text{ and } \rho'(\boldsymbol{\eta}_{\text{opt}}) \leq 0 \text{ and } \rho''(\boldsymbol{\eta}_{\text{opt}}) > 0 \ (23.4) \end{cases} \end{cases} \tag{23}$$

When condition (23.1) or condition (23.2) is met, it is determined as H_0; when condition (23.3) or condition (23.4) is met, it is determined as H_1.

V. Experimental Verification and Performance Analysis

In this section, experiments are conducted based on real sea clutter data to verify the effectiveness of the proposed mRMR-Tri-ConcaveHull detector. In the experiments, IPIX Radar data collected in 1993 and 1998 by Professor Haykin of Canada McMaster University were used [38]. IPIX Radar can transmit horizontal polarization and vertical polarization electromagnetic waves and uses two linear receivers to complete the horizontal and vertical reception. Therefore, radar echo data of HH, HV, VH, and VV polarities can usually be obtained.

In the experiments, we use 10 datasets collected in 1993 and 10 datasets collected in 1998. During the data collection, there were certain differences between the radar working place, data acquisition parameters, and cooperative targets. When collecting data in 1993, the radar was set up on a 30 m high cliff near Dartmouth, Nova Scotia, on the east coast of Canada. The radar was directed toward the Atlantic Ocean. The target to be detected was a floating ball wrapped in aluminum wire with a diameter of 1 m. The operating frequency of the radar was 9.3 GHz, the beam width was 0.9°, and the range resolution was 30 m. The radar operated in dwell mode with a pulse repetition frequency of 1000 Hz and dwell time of approximately 131 s. Each group of data contains 14 range cells. In 1998, the IPIX Radar was placed in Grimsby, Ontario, to collect a new set of data. The radar was set at a height of 20 m, and the target to be measured was a floating boat. The range resolution was 30 m, the pulse repetition frequency was 1000 Hz, and the dwell time was 60 s, including 28 range cells.

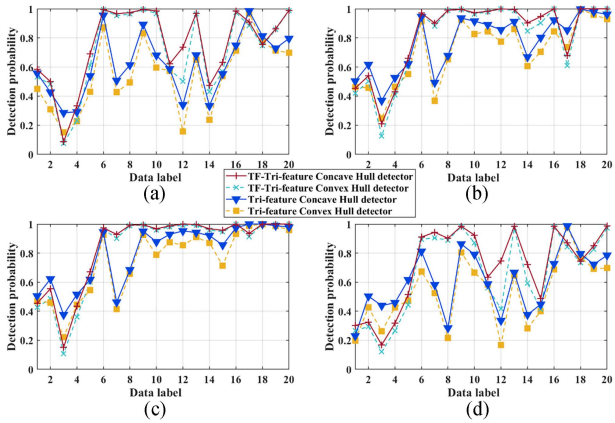

Fig. 7. Detection probability of the convex hull detector and concave hull detector without optimal feature selection under four polarizations for 20 datasets with $N = 512$, $P_F = 0.001$. (a) HH. (b) HV. (c) VH. (d) VV.

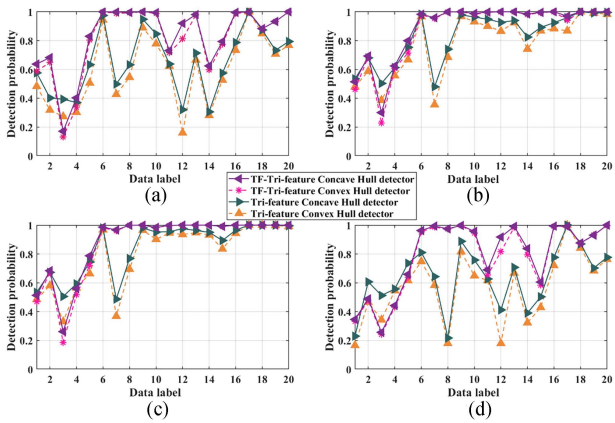

Fig. 8. Detection probability of the convex hull detector and concave hull detector without optimal feature selection under four polarizations for 20 datasets with $N = 1024$, $P_F = 0.001$. (a) HH. (b) HV. (c) VH. (d) VV.

A. Performance of the 3-D Convex Hull Detector and 3-D Concave Hull Detector Without Optimal Feature Selection

In this section, the RAA-RDPH-RVE and RI-NR-MS are input into the convex hull detector and our proposed 3-D concave hull detector, respectively, to compare the detection performance. Among them, the Tri-feature Convex Hull (TFC-H) detector is the RAA-RDPH-RVE convex hull detector from [15], the TF-Tri-feature Convex Hull (T-T-FCH) detector is the RI-NR-MS convex hull detector in [16], and the Tri-feature Concave Hull detector and TF-Tri-feature Concave Hull detector are 3-D FAC concave hull detectors using RAA-RDPH-RVE and RI-NR-MS, respectively. In the experiment, we set the false alarm rate to 0.001. The detection probabilities of the four detectors are shown in Figs. 7 and 8.

As shown in Figs. 7 and 8, based on 20 datasets, the TF-Tri-feature Concave Hull detector and the Tri-feature Concave Hull detector are superior to the TFC-H detector and the T-T-FCH

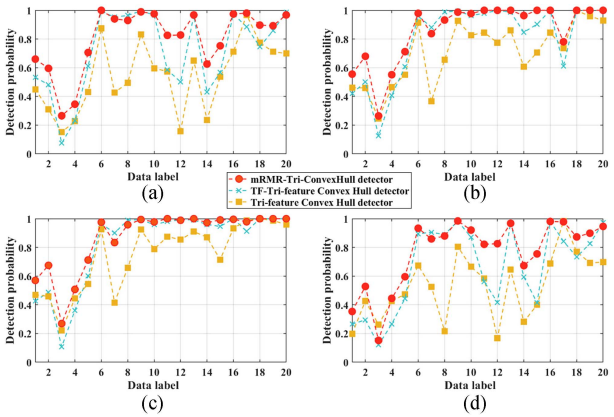

Fig. 9. Detection probability of three convex hull detectors under four polarizations for 20 datasets with $N = 512$, $P_F = 0.001$. (a) HH. (b) HV. (c) VH. (d) VV.

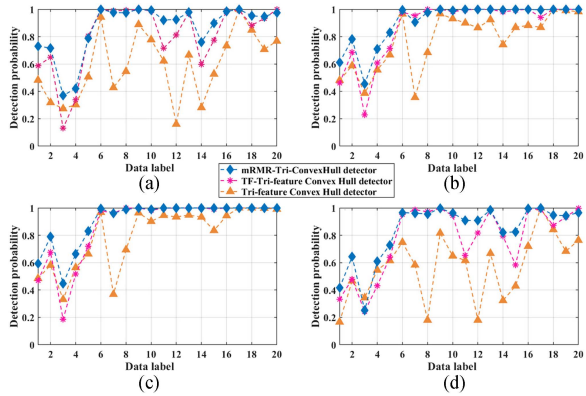

Fig. 10. Detection probability of three convex hull detectors under four polarizations for 20 datasets with $N = 1024$, $P_F = 0.001$. (a) HH. (b) HV. (c) VH. (d) VV.

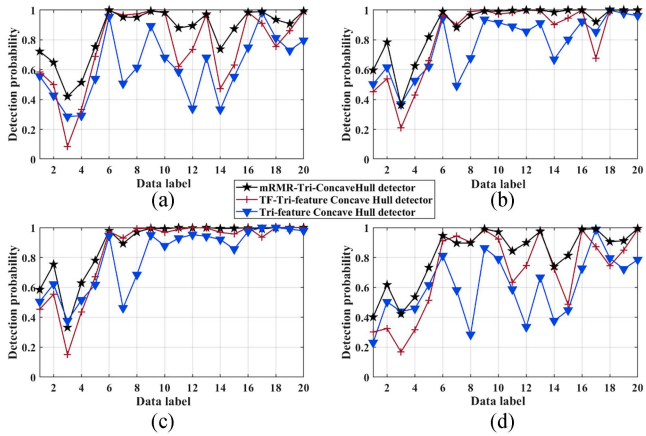

Fig. 11. Detection probability of three concave hull detectors under four polarizations for 20 datasets with $N = 512$, $P_F = 0.001$. (a) HH. (b) HV. (c) VH. (d) VV.

detector, respectively. This result indicates that the performance of the proposed 3-D FAC concave hull detector is superior to that of the existing convex hull detectors because the concave hull we generate is completed on the basis of the convex hull through internal digging and external filling. The concave hull is a part of the convex hull, and the volume of the concave hull must be smaller than the volume of the convex hull. Therefore, the detection performance of our proposed 3-D FAC concave hull detector is better than that of the convex hull detectors. On the other hand, the detection performance of the concave hull detector for different datasets is improved to different extents, with a maximum increase of 32.90% because the improvement of the detection performance depends on whether the generated original convex hull judgment area can tightly wrap the sea clutter feature vectors. If there is a larger gap area in the convex hull, the target feature vectors that fall in the gap area will be incorrectly identified as clutter feature vectors. Whereas our concave hull learning algorithm can dig out these gap areas under the condition of meeting the CFAR. These target feature vectors can be correctly identified in the concave hull, so the performance of the concave hull detectors will improve more. When the detection probability of the convex hull is 1, the detection probability of the concave hull is the same as that of the convex hull, and the performance improvement is 0.

B. Performance of the 3-D Convex Hull Detector With Different Features

In this section, the RAA-RDPH-RVE, RI-NR-MS, and the optimal three features selected by the mRMR algorithm are input to the convex hull detector. Among them, the TFC-H detector [15] and T-T-FCH detector [16] are convex hull detectors using the RAA-RDPH-RVE and RI-NR-MS, respectively. The mRMR-Tri-ConvexHull detector is a convex hull detector that uses the mRMR to obtain three optimal features. In the experiment, we set the false alarm rate to 0.001, and the detection probabilities of the four detectors are shown in Figs. 9 and 10.

As shown in Figs. 9 and 10, based on 20 datasets and compared with the other two algorithms, the mRMR-Tri-ConvexHull detector can essentially achieve the best detection performance. Compared with the TFC-H detector, the mRMR-Tri-ConvexHull detector can improve the detection performance by up to 77.59%, and compared with the T-T-FCH detector, the mRMR-Tri-ConvexHull detector can improve the detection performance by up to 40.86%. These results show that in the convex hull detector, the mRMR can improve the robustness of the detection performance.

C. Performance of the 3-D FAC Concave Hull Detector With Different Features

In this section, the RAA-RDPH-RVE, RI-NR-MS, and the optimal three features selected by the mRMR algorithm are input into our 3-D FAC concave hull detector. Among them, the Tri-feature Concave Hull detector and TF-Tri-feature Concave Hull detector are concave hull detectors using the RAA-RDPH-RVE and RI-NR-MS, respectively. The mRMR-Tri-ConcaveHull detector is a concave hull detector that uses the mRMR to obtain three optimal features. In the experiment, we set the false alarm rate to 0.001. The detection probabilities of the four detectors are shown in Figs. 11 and 12.

TABLE I
AVERAGE DETECTION PROBABILITIES OF THE SIX DETECTORS ON THE 20 DATA SETS WITH FOUR POLARIZATIONS

Detector			N	HH	HV	VH	VV	Avg P_d
Convex	Without mRMR	Tri-feature Convex Hull detector[15]	512	0.577	0.736	0.776	0.569	0.665
			1024	0.622	0.797	0.813	0.598	0.708
		TF-Tri-feature Convex Hull detector[16]	512	0.747	0.826	0.842	0.706	0.780
			1024	0.821	0.882	0.877	0.789	0.842
	With mRMR	mRMR-Tri-ConvexHull detector	512	0.810	0.861	0.870	0.769	0.828
			1024	0.866	0.912	0.913	0.839	0.883
Concave	Without mRMR	Tri-feature Concave Hull detector	512	0.636	0.782	0.814	0.620	0.713
			1024	0.660	0.831	0.846	0.646	0.746
		TF-Tri-feature Concave Hull detector	512	0.772	0.841	0.858	0.725	0.799
			1024	0.838	0.890	0.887	0.796	0.853
	With mRMR	mRMR-Tri-ConcaveHull detector	512	**0.855**	**0.896**	**0.894**	**0.824**	**0.867**
			1024	**0.898**	**0.936**	**0.936**	**0.877**	**0.912**

The bold values represent the detection probability of our proposed algorithm. Compared with other algorithms, the detection probability of our proposed algorithm is the best, so it is represented by the bold values.

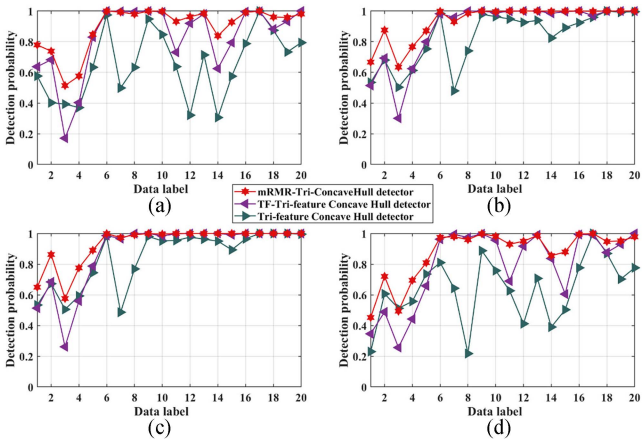

Fig. 12. Detection probability of three concave hull detectors under four polarizations for 20 datasets with $N = 1024$, $P_F = 0.001$. (a) HH. (b) HV. (c) VH. (d) VV.

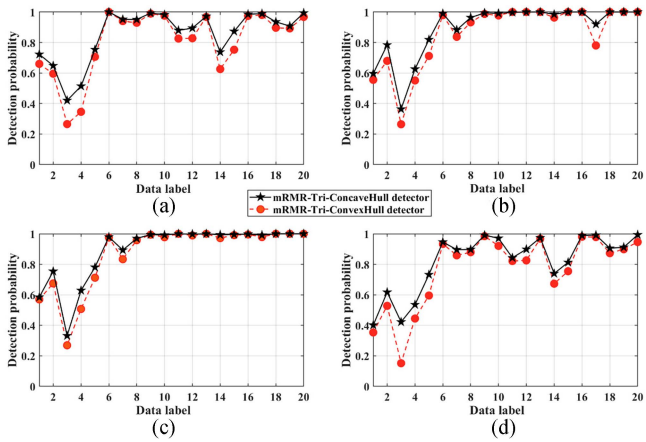

Fig. 13. Detection probability of the mRMR-Tri-ConcaveHull detector and the mRMR-Tri-ConvexHull detector under four polarizations for 20 datasets with $N = 512$, $P_F = 0.001$. (a) HH. (b) HV. (c) VH. (d) VV.

As shown in Figs. 11 and 12, on 20 datasets, the mRMR-Tri-ConcaveHull detector essentially achieves the best detection performance compared with the other two detectors. Compared with the Tri-feature Concave Hull detector, mRMR-Tri-ConcaveHull detector can increase the detection performance by up to 74.24%, and the mRMR-Tri-ConcaveHull detector can increase the detection performance by up to 34.32% compared with the TF-Tri-feature Concave Hull detector. These results indicate that in the 3-D FAC concave hull detector, the mRMR can improve the robustness of detection performance.

D. Performance of the mRMR-Tri-ConvexHull Detector and mRMR-Tri-ConcaveHull Detector

From Section V-A to V-C, we can see that both the mRMR and the 3-D concave hull detector can improve the detection performance. In this section, with the help of the mRMR, we input three optimal features into the convex hull detector and the concave hull detector. We compare the mRMR-Tri-ConvexHull detector with the mRMR-Tri-ConcaveHull detector. In the experiment,

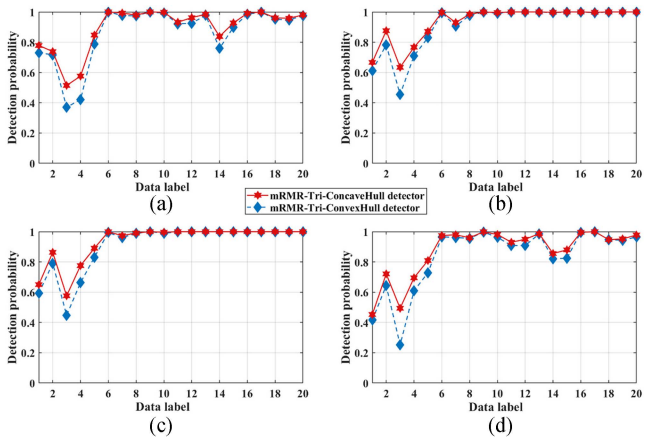

Fig. 14. Detection probability of the mRMR-Tri-ConcaveHull detector and the mRMR-Tri-ConvexHull detector under four HH s for 20 datasets with $N = 1024$, $P_F = 0.001$. (a) HH. (b) HV. (c) VH. (d) VV.

TABLE II
COMPUTATIONAL COMPLEXITY OF THE MRMR-TRI-CONCAVEHULL DETECTOR AND CONVEX HULL DETECTOR

Detector		Computational complexity
mRMR-Tri-ConcaveHull detector	mRMR	$O(10)$
	Tri-ConcaveHull	$O(N_f * vernum * Qlog(vernum) + dig\_num(Q^2 * log(vernum) + 4(H+S)))$
convex hull detector		$O(N_f * vernum * Qlog(vernum))$

we set the false alarm rate to 0.001. The detection probabilities of the four detectors are shown in Figs. 13 and 14.

From Figs. 13 and 14, we can see that the detection performance of the mRMR-Tri-ConcaveHull detector is better than that of the mRMR-Tri-ConvexHull detector on the 20 datasets. The mRMR-Tri-ConcaveHull detector can further improve the detection performance by using the combination of the optimal feature selection and concave hull.

E. Performance of the Six Detectors

The TFC-H detector [15], T-T-FCH detector [16], mRMR-Tri-ConvexHull detector, Tri-feature Concave Hull detector, TF-Tri-feature Concave Hull detector, and mRMR-Tri-ConcaveHull detector run on 20 datasets under four polarizations with $N = 512$ and 1024, $P_F = 0.001$. Table I lists the average detection probabilities of six detectors on 20 datasets with four polarizations in the IPIX radar database, where the averages at each polarization and at the four polarizations are listed separately. As seen in Table I, the detection performance of 3-D FAC concave hull detector is better than that of the convex hull detectors. In addition, the mRMR can also improve the detection performance to a certain extent. Combining the mRMR with the 3-D FAC concave hull detector, the proposed mRMR-Tri-ConvaveHull detector has the best detection performance.

F. Computational Complexity of the Proposed mRMR-Tri-ConcaveHull Detector and Convex Hull Detector

Table II shows the computational complexity of the proposed mRMR-Tri-ConcaveHull detector and convex hull detector. Among them, N_f represents the number of false alarm points, dig_num is the number of internal digging operations, H is the number of clutter feature vectors outside $\Omega_{i,j}$, S is the number of points in set J_s, Q is the total number of sea clutter samples, and vernum is the number of vertex of convex hull. From Table II, it can be seen that the proposed mRMR-Tri-ConcaveHull detector is slightly more complex than the convex hull detector. In the above experiments, the feasibility of the proposed mRMR-Tri-ConcaveHull detector is verified.

TABLE III
AVERAGE DETECTION PROBABILITIES OF THE TEN FEATURE-BASED DETECTORS ON THE 20 DATA SETS WITH FOUR POLARIZATIONS

Detector	N	HH	HV	VH	VV	Avg P_d
F-B[9]	512	0.223	0.404	0.448	0.241	0.329
	1024	0.301	0.536	0.576	0.328	0.435
DF-F-B[17]	512	0.471	0.681	0.692	0.427	0.568
	1024	0.481	0.723	0.734	0.447	0.596
S-B[20]	512	0.526	0.690	0.744	0.530	0.623
	1024	0.517	0.732	0.757	0.505	0.628
TFC-H[15]	512	0.577	0.736	0.776	0.569	0.665
	1024	0.622	0.797	0.813	0.598	0.708
P-B[18]	512	0.658	0.839	0.848	0.668	0.754
	1024	0.748	0.874	0.876	0.735	0.808
T-T-FCH[16]	512	0.747	0.826	0.842	0.706	0.780
	1024	0.821	0.882	0.877	0.789	0.842
FF-F-B[19]	512	0.756	0.859	0.866	0.743	0.806
	1024	0.805	0.887	0.883	0.791	0.841
F-C-B[17]	512	0.807	0.880	0.888	0.788	0.841
	1024	0.841	0.920	0.914	0.839	0.879
K-B[21]	512	0.819	0.902	0.907	0.806	0.858
	1024	0.884	0.936	0.931	0.868	0.905
M-T-C	512	**0.855**	**0.896**	**0.894**	**0.824**	**0.867**
	1024	**0.898**	**0.936**	**0.936**	**0.877**	**0.912**

The bold values represent the detection probability of our proposed algorithm. Compared with other algorithms, the detection probability of our proposed algorithm is the best, so it is represented by the bold values.

G. Performance of the mRMR-Tri-ConvexHull Detector and Nine Feature-Based Detectors

The existing 9 feature-based detectors and the proposed detectors run on 20 datasets under four polarizations with $N = 512$ and 1024, $P_F = 0.001$. Table III lists the average detection probabilities of 10 detectors on 20 datasets with four polarizations in the IPIX radar database, where the averages at each polarization and at the four polarizations are listed separately. As seen in Table III, the proposed mRMR-Tri-ConvaveHull (M-T-C) detector has the best detection performance. The fractal-based (F-B) detector [9] only utilizes a single feature, and its detection performance is the worst. The second worst is the direct feature-fusion-based (DF-F-B) detector [17], as it causes serious performance losses in the process of direct feature fusion. For SVM-based (S-B) detector [20], TFC-H detector [15], and T-T-FCH detector [16], they use 3-D features, which cannot achieve the highest recognition of target features and sea clutter features in 3-DFS, thus their detection ability is limited. For PCA-based (P-B) detector [18] and feature-compression-based (F-C-B) detectors [17], they extract or compress three-dimensional features from the high dimensional space and use convex hulls to match the concave distribution of sea clutter, and this inevitably enlarge the judgment area and considerably decreases the detection probability. Due to prior information, Fast feature-fusion-based (FF-F-B) detector [19] and KNN-based (K-B) detector [21] achieve a good performance. Moreover, our proposed M-T-C

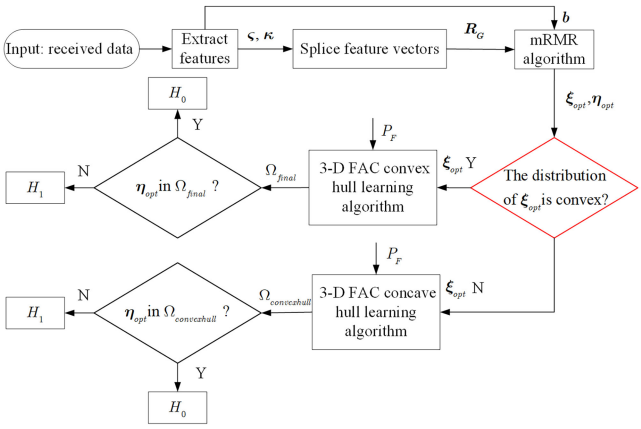

Fig. 15. Flow chart of the operation that infers the clutter feature distribution after the mRMR based on the mRMR-Tri-ConvexHull detector and mRMR-Tri-ConcaveHull detector.

detector not only uses the prior information but also compensates the disadvantage of the concave hull, resulting in the optimal performance.

H. Experimental Conclusion

The distribution of sea clutter features in the 3-DFS is convex or concave. If the distribution is convex, we use the mRMR-Tri-ConvexHull detector; otherwise, we use the mRMR-Tri-ConcaveHull detector. Combining the two detectors, we add the operation that infers the clutter feature distribution after the mRMR, as shown in Fig. 15.

As shown in Fig. 15, after selecting the optimal three feature vectors with the mRMR, we determine whether the distribution of clutter feature vectors is convex. On the condition that the distribution is convex, we use the convex hull learning algorithm to form a convex judgment area $\Omega_{\text{convexhull}}$. If η_{opt} is inside $\Omega_{\text{convexhull}}$, it will be judged as clutter; otherwise, it will be judged as a target. On the condition that the distribution is concave, we use the concave hull learning algorithm to form the concave judgment area Ω_{final}. If η_{opt} is inside Ω_{final}, it will be judged as clutter; otherwise, it will be judged as a target.

VI. Conclusion

The detection of small floating targets in sea clutter has always been a difficult problem due to complicated sea clutter and the low RCS of small targets. The high-dimensional feature detector is a trend, whereas the distribution of the feature is hard to define. In this article, we use the mRMR to choose the features for 3-DFS from the HDFS and measure the distribution of the 3-D features. In most cases, the distribution is concave. Therefore, we propose the 3-D FAC concave hull detector to meet the concave distribution of features. Combining the mRMR and the 3-D FAC concave hull detector, we propose the mRMR-Tri-ConcaveHull detector. The simulated results based on the measured data show that the proposed mRMR-Tri-ConcaveHull detector has better detection performance than the existing nine feature-based detectors, which provides a new idea for target detection in sea clutter.

According to research works [39], [40], IPIX radar is an X-band radar, but in practical applications, the accuracy and stability of radar detection may be affected by interference factors such as rain clutter. Rainfall can blur the wave signatures, which may negatively impact the use of X-band marine radar to measure ocean surface parameters. Ensuring that marine radars have efficient and robust detection capabilities in any weather condition is a challenging problem that we will explore in the future.

References

[1] P. Huang, Z. Zou, X. G. Xia, X. Liu, G. Liao, and Z. Xin, "Multichannel sea clutter modeling for spaceborne early warning radar and clutter suppression performance analysis," *IEEE Trans. Geosci. Remote Sens.*, vol. 59, no. 10, pp. 8349–8366, Oct. 2021.

[2] S. Xu, J. Zhu, J. Jiang, and P. Shui, "Sea-surface floating small target detection by multifeature detector based on isolation forest," *IEEE J. Sel. Topics Appl. Earth Observ. Remote Sens.*, vol. 14, pp. 704–715, 2021.

[3] W. Zhao, M. Jin, G. Cui, and Y. Wang, "Eigenvalues-based detector design for radar small floating target detection in sea clutter," *IEEE Geosci. Remote Sens. Lett.*, vol. 19, 2022, Art. no. 3509105.

[4] Y. Yan, G. Wu, Y. Dong, and Y. Bai, "An improved MSR-based data-driven detection method using smoothing pre-processing," *IEEE Signal Process. Lett.*, vol. 28, pp. 444–448, 2021.

[5] K. Yan, Y. Bai, H. Wu, and X. Zhang, "Robust target detection within sea clutter based on graphs," *IEEE Trans. Geosci. Remote Sens.*, vol. 57, no. 9, pp. 7093–7103, Sep. 2019.

[6] Y. Shi, "Three GLRT detectors for range distributed target in grouped partially homogeneous radar environment," *Signal Process.*, vol. 135, pp. 121–131, 2017.

[7] Y. Yan, G. Wu, Y. Dong, and Y. Bai, "Floating small target detection in sea clutter using mean spectral radius," *IEEE Geosci. Remote Sens. Lett.*, vol. 19, 2022, Art. no. 4023405.

[8] L. Suo, C. Zhao, and X. Hu, "Sea-surface floating small target detection based on joint features," in *Proc. IEEE 5th Inf. Technol. Mechatronics Eng. Conf.*, 2020, pp. 882–887.

[9] J. Hu, J. Gao, K. Yao, and U. Kim, "Detection of low observable targets within sea clutter by structure function based multifractal analysis," in *Proc. IEEE Int. Conf. Acoust., Speech, Signal Process.*, 2005, vol. 5, pp. v/709–v/712.

[10] T. Lo, H. Leung, J. Litva, and S. Haykin, "Fractal characterization of sea-scattered signals and detection of sea-surface targets," *Proc. Inst. Elect. Eng.*, vol. 140, pp. 243–250, 1993.

[11] X. Chen et al., "Detection of low observable moving target in sea clutter via fractal characteristics infractional Fourier transform domain," *Inst. Eng. Technol. Radar Sonar Navig.*, vol. 7, no. 6, pp. 635–651, 2013.

[12] D. Li and P. Shui, "Floating small target detection in sea clutter via normalised Doppler power spectrum," *Inst. Eng. Technol. Radar Sonar Navigat.*, vol. 10, no. 4, pp. 699–706, Mar. 2016.

[13] Y. Jin, Z. Chen, L. Fan, and C. Zhao, "No access spectral kurtosis–based method for weak target detection in sea clutter by microwave coherent radar," *J. Atmospheric Ocean. Technol.*, vol. 32, no. 2, pp. 310–317, 2015.

[14] Y. Shi, X. Xie, and D. Li, "Range distributed floating target detection in sea clutter via feature-based detector," *IEEE Geosci. Remote Sens. Lett.*, vol. 13, no. 12, pp. 1847–1850, Dec. 2016.

[15] P.-L. Shui, D.-C. Li, and S.-W. Xu, "Tri-feature-based detection of floating small targets in sea clutter," *IEEE Trans. Aerosp. Electron. Syst.*, vol. 50, no. 2, pp. 1416–1430, Apr. 2014.

[16] S.-N. Shi and P.-L. Shui, "Sea-surface floating small target detection by one-class classifier in time-frequency feature space," *IEEE Trans. Geosci. Remote Sens.*, vol. 56, no. 11, pp. 6395–6411, Nov. 2018.

[17] P. Shui, Z. Guo, and S. Shi, "Feature-compression-based detection of sea-surface small targets," *IEEE Access*, vol. 8, pp. 8371–8385, 2020.

[18] T. Gu, "Detection of small floating targets on the sea sur-face based on multi-features and principal component analysis," *IEEE Geosci. Remote Sens. Lett.*, vol. 17, no. 5, pp. 809–813, May 2020.

[19] Z.-X. Guo, X.-H. Bai, J.-Y. Li, and P.-L. Shui, "Fast detection of small targets in high-resolution maritime radars by feature normalization and fusion," *IEEE J. Ocean. Eng.*, vol. 47, no. 3, pp. 736–750, Jul. 2022.

[20] Y. Li, P. Xie, Z. Tang, T. Jiang, and P. Qi, "SVM-based sea-surface small target detection: A false-alarm-rate-controllable approach," *IEEE Geosci. Remote Sens. Lett.*, vol. 16, no. 8, pp. 1225–1229, Aug. 2019.

[21] Z.-X. Guo and P.-L. Shui, "Anomaly based sea-surface small target detection using K-nearest neighbor classification," *IEEE Trans. Aerosp. Electron. Syst.*, vol. 56, no. 6, pp. 4947–4964, Dec. 2020.
[22] L. Wen, J. Ding, C. Zhong, and Q. Guo, "Modeling of correlated complex sea clutter using unsupervised phase retrieval," *IEEE Trans. Geosci. Remote Sens.*, vol. 59, no. 1, pp. 228–239, Jan. 2021.
[23] X. Li, P.-L. Shui, Z.-D. Zhang, Y.-S. Zhang, and S.-W. Xu, "External calibration of P-band island-based sea clutter measurement radar on the sea surface," *IEEE Trans. Geosci. Remote Sens.*, vol. 59, no. 7, pp. 5711–5720, Jul. 2021.
[24] Y. Yuan, J. Fang, X. Lu, and Y. Feng, "Remote sensing image scene classification using rearranged local features," *IEEE Trans. Geosci. Remote Sens.*, vol. 57, no. 3, pp. 1779–1792, Mar. 2019.
[25] Y. Shi, Y. Guo, T. Yao, and Z. Liu, "Sea-surface small floating target recurrence plots false alarm controllable classification based on CNN," *IEEE Trans. Geosci. Remote Sens.*, vol. 60, 2022, Art no. 5115713.
[26] P. Li and O. Niggemann, "Improving clustering based anomaly detection with concave hull: An application in fault diagnosis of wind turbines," in *Proc. IEEE 14th Int. Conf. Ind. Inform.*, 2016, pp. 463–466.
[27] J. Guan et al., "Detection of small targets on sea surface based on 3-D concave hull learning algorithm," *J. Electron. Inf. Technol.*, vol. 44, pp. 1–9, 2022.
[28] N. Almusallam, Z. Tari, J. Chan, A. Fahad, A. Alabdulatif, and M. Al-Naeem, "Towards an unsupervised feature selection method for effective dynamic features," *IEEE Access*, vol. 9, pp. 77149–77163, 2021.
[29] P. Zhou, P. Li, S. Zhao, and X. Wu, "Feature interaction for streaming feature selection," *IEEE Trans. Neural Netw. Learn. Syst.*, vol. 32, no. 10, pp. 4691–4702, Oct. 2021.
[30] P. N. da Silva, A. Plastino, F. Fabris, and A. A. Freitas, "A novel feature selection method for uncertain features: An application to the prediction of pro-/anti-longevity genes," *IEEE/Assoc. Comput. Machinery Trans. Comput. Biol. Bioinf.*, vol. 18, no. 6, pp. 2230–2238, Nov./Dec. 2021.
[31] G. S. Thejas, R. Garg, S. S. Iyengar, N. R. Sunitlha, P. Badrinath, and S. Chennupati, "Metric and accuracy ranked feature inclusion: Hybrids of filter and wrapper feature selection approaches," *IEEE Access*, vol. 9, pp. 128687–128701, 2021.
[32] H. Peng, F. Long, and C. Ding, "Feature selection based on mutual information criteria of max-dependency, max-relevance, and min-redundancy," *IEEE Trans. Pattern Anal. Mach. Intell.*, vol. 27, no. 8, pp. 1226–1238, Aug. 2005.
[33] G. Wang, F. Lauri, and A. H. E. Hassani, "Feature selection by mRMR method for heart disease diagnosis," *IEEE Access*, vol. 10, pp. 100786–100796, 2022.
[34] Y. Chen, T. Jiang, H. Liu, Y. Li, and Z. Yu, "Event recognition system based on fiber Bragg grating and mRMR-CWCs-SCN," *IEEE Sensors J.*, vol. 21, no. 22, pp. 26132–26139, Nov. 2021.
[35] P.-L. Shui and Y.-L. Shi, "Subband ANMF detection of moving targets in sea clutter," *IEEE Trans. Aerosp. Electron. Syst.*, vol. 48, no. 4, pp. 3578–3593, Oct. 2012.
[36] D. Li and P. Shui, "Floating small target detection in sea clutter via normalised Hurst exponent," *Electron. Lett.*, vol. 50, no. 17, pp. 1240–1242, 2014.
[37] E. J. Kelly, "An adaptive detection algorithm," *IEEE Trans. Aerosp. Electron. Syst.*, vol. AES-22, no. 2, pp. 115–127, Mar. 1986.
[38] "The McMaster IPIX radar sea clutter database," Accessed: Jul. 1, 2001. [Online]. Available: http://soma.ece.mcmaster.ca/ipix
[39] W. Huang, X. Liu, and E. W. Gill, "Ocean wind and wave measurements using X-band marine radar: A comprehensive review," *Remote Sens.*, vol. 9, no. 12, 2017, Art. no. 1261.
[40] X. Chen and W. Huang, "Identification of rain and low-backscatter regions in X-band marine radar images: An unsupervised approach," *IEEE Trans. Geosci. Remote Sens.*, vol. 58, no. 6, pp. 4225–4236, Jun. 2020.

Yanling Shi was born in 1983. She received the B.E. and Ph.D. degrees in signal and information processing from the Xidian University, Xi'an, China, in 2006 and 2011, respectively.

She is currently an Associate Professor with the School of Telecommunications and Information Engineering, Nanjing University of Posts and Telecommunications, Nanjing, China. Her research interests include radar target detection, scattering of sea clutter, and deep learning in radar signal processing.

Yuefeng Hu was born in 1999. She is currently working toward the Master's degree in electronics and communication engineering with the Nanjing University of Posts and Telecommunications, Nanjing, China.

Her research interests include information geometry and radar target detection.